



## OPEN ACCESS

## EDITED BY

Takashi Nakagawa,  
Kobe University, Japan

## REVIEWED BY

Frederic Deschamps,  
Academia Sinica, Taiwan  
Carsten Rott,  
The University of Utah, United States

## \*CORRESPONDENCE

Véronique Van Elewyck,  
✉ [elewyck@apc.in2p3.fr](mailto:elewyck@apc.in2p3.fr)  
Edouard Kaminski,  
✉ [kaminski@ipgp.fr](mailto:kaminski@ipgp.fr)

## SPECIALTY SECTION

This article was submitted to Solid Earth Geophysics, a section of the journal *Frontiers in Earth Science*

RECEIVED 31 July 2022

ACCEPTED 09 February 2023

PUBLISHED 14 March 2023

## CITATION

Maderer L, Kaminski E, Coelho JAB, Bourret S and Van Elewyck V (2023), Unveiling the outer core composition with neutrino oscillation tomography. *Front. Earth Sci.* 11:1008396. doi: 10.3389/feart.2023.1008396

## COPYRIGHT

© 2023 Maderer, Kaminski, Coelho, Bourret and Van Elewyck. This is an open-access article distributed under the terms of the [Creative Commons Attribution License \(CC BY\)](https://creativecommons.org/licenses/by/4.0/). The use, distribution or reproduction in other forums is permitted, provided the original author(s) and the copyright owner(s) are credited and that the original publication in this journal is cited, in accordance with accepted academic practice. No use, distribution or reproduction is permitted which does not comply with these terms.

# Unveiling the outer core composition with neutrino oscillation tomography

Lukas Maderer<sup>1</sup>, Edouard Kaminski<sup>2\*</sup>, João A. B. Coelho<sup>1,3</sup>, Simon Bourret<sup>1</sup> and Véronique Van Elewyck<sup>1,4\*</sup>

<sup>1</sup>Astroparticule et Cosmologie, CNRS, Université Paris Cité, Paris, France, <sup>2</sup>Institut de Physique du Globe de Paris, CNRS, Université Paris Cité, Paris, France, <sup>3</sup>CNRS/IN2P3, IJCLab, Université Paris-Saclay, Orsay, France, <sup>4</sup>Institut Universitaire de France, Paris, France

In the last 70 years, geophysics has established that the Earth's outer core is an FeNi alloy containing a few percent of light elements, whose nature and amount remain controversial. Besides the classical combinations of silicon and oxygen, hydrogen has been advocated as the only light element that could account alone for both the core density and velocity profiles. Here we show how this question can be addressed from an independent viewpoint, by exploiting the tomographic information provided by atmospheric neutrinos, weakly-interacting particles produced in the atmosphere and constantly traversing the Earth. We evaluate the potential of the upcoming generation of atmospheric neutrino detectors for such a measurement, showing that they could efficiently detect the presence of 1 wt% hydrogen in the Earth's core in 50 years of concomitant data taking. We then identify the main requirements for a next-generation detector to perform this measurement in a few years timescale, with the further capability to efficiently discriminate between FeNiH and FeNiSi<sub>x</sub>O<sub>y</sub> core composition models in less than 15 years.

## KEYWORDS

neutrinos, oscillations, Earth tomography, outer core composition, hydrogen, KM3NeT/ORCA, hyper-Kamiokande

## 1 Introduction

The determination of the composition of the Earth core is a long-standing debate in Earth sciences [e.g., Birch (1961); Poirier (1994); Hirose et al. (2013); McDonough (2003)]. Seismology combined with experimental petrology shows that the inclusion of a few percent of light elements is required to account for the density and seismic velocity profiles in the core, e.g., PREM (Dziewonski and Anderson, 1981). Si, O, S, C, and H (and some of their combinations) are the most popular elements that have been considered so far. The precise nature of the light elements in the core however remains elusive, and various combinations of, e.g., Si and O (Kaminski and Javoy, 2013; Badro et al., 2015), can equally fit PREM. Hydrogen, the most abundant element in the proto-solar nebula, has received a renewed interest in the past years based on high-pressure/high-temperature experiments that confirmed the possibility to put a significant amount of H in the core (Sakamaki et al., 2009; Tagawa et al., 2021). Furthermore, it is the only candidate that could account for both the density and velocity profiles in the core without the need for any additional light element (Umamoto and Hirose, 2015; Sakamaki et al., 2016; Yuan and Steinle-Neumann, 2020).

The presence of light elements in the core bears important consequences for the dynamics and formation of the Earth and of its magnetic field [Hirose et al. (2013)]. The latter rises from convection in the liquid outer core, a key question being the mechanism allowing the convective process to be efficient enough to sustain a geodynamo. Because light elements partition in the liquid phase during crystallization of the inner core, they increase the intensity of convection in the outer core, that becomes then a thermo-chemical process. This in turn improves the efficiency of cooling of the core, thereby decreasing its temperature and causing further delay in the crystallization process. Determining the precise composition of the core is therefore of prime importance to better understand the conditions of its segregation, and more generally to help discriminate different scenarios of Earth formation. For example, the relative amount of oxygen to silicon depends both on pressure and temperature conditions during iron formation, and on the nature of the material that formed the Earth. An oxygen-rich core would be expected if carbonaceous chondrites were the building blocks of the Earth, whereas a silicon-rich core would rather correspond to Enstatite chondrites.

If hydrogen is the dominant light element in the core, a very different scenario would be at play as the Mg/Si ratio of the mantle—which is non-chondritic—will be very close to that of the bulk Earth. A hydrogen-rich core would furthermore completely change the H<sub>2</sub>O bulk content of the Earth, increasing it up to 75 equivalent of the ocean content (Tagawa et al., 2021). Up to now however there has been no method available to directly constrain the amount of H in the core. The aim of the present study is to show how the development of high-performance detectors of atmospheric neutrinos opens a new path to independently constrain the composition of the core and test the FeNiH hypothesis in particular.

Neutrinos are neutral elementary particles that exist in three flavors: electron ( $e$ ), muon ( $\mu$ ) and tau ( $\tau$ ). Because they feel only the weak interaction, they can traverse and emerge from very dense media, including the Earth itself, without losing energy during their propagation. The interactions of cosmic rays with the atmosphere generate an abundant and ubiquitous flux of energetic neutrinos, which undergo flavor oscillations while crossing the Earth (Fukuda et al., 1998). The probability of their flavor transition depends on the neutrino energy and path length, but also on the density of electrons  $n_e$  in the traversed medium (Wolfenstein, 1978; Mikheyev and Smirnov, 1985). Because of its dependence in  $n_e$ , this effect is key in accessing chemical properties of the traversed medium through neutrino oscillation physics. Assuming an Earth's radial structure and composition,  $n_e$  as a function of  $r$ , the radial distance from the center of the Earth, is given by

$$n_e(r) = \frac{Z}{A}(r) \times \rho(r) \times \mathcal{N}_A, \quad (1)$$

where  $\mathcal{N}_A$  is the Avogadro number,  $\rho$  is the mass density, and  $Z/A$  is the proton-to-nucleon ratio defined as:

$$\frac{Z}{A} = \sum_i w_i \frac{Z_i}{A_i}, \quad (2)$$

where  $Z_i$ ,  $A_i$  and  $w_i$  are respectively the local atomic number, standard atomic weight and weight fraction of element  $i$  of the material. Chemical elements with different  $Z/A$  will therefore

generate distinct signals in the neutrino oscillation pattern for a given mass density. The signature of these oscillations in the atmospheric neutrino signal observed at a detector can thus reveal the nature of the matter they interacted with.

While this method of Earth tomography has been conceptually explored in different contexts since the 1980s [see, e.g., Ermilova et al. (1986); Nicolaidis (1988); Nicolaidis et al. (1991); Ohlsson and Winter (2001); Ohlsson and Winter (2002); Lindner et al. (2003); Winter (2006) and references therein], only now does the upcoming generation of atmospheric neutrino detectors provide a concrete opportunity to evaluate its capability of probing the density and/or composition of the deep Earth. Oscillation tomography with atmospheric neutrinos has been recently discussed by several authors (Rott et al., 2015; Winter 2016; Bourret et al., 2018; Bourret and Van Elewyck, 2019; D'Olivo et al., 2020; Kumar and Agarwalla, 2021; Denton and Pestes, 2021; Kelly et al., 2022; Capozzi and Petcov, 2022; D'Olivo Saez et al., 2022), with a variety of approaches in the treatment of the neutrino signal and in the targeted geophysical observables. In this study, we propose to re-examine the relevance and potential of this method for the characterization of the Earth's core composition, with a specific focus on its capacity to identify and quantify the presence of Hydrogen in the core. This topical question for the geoscience community indeed appears as a promising area of application of neutrino oscillation tomography thanks to the very large  $Z/A$  of H compared to Fe and other light elements.

Section 2 describes the theoretical background, the methods and inputs used for the computations that support the present study. Our main results on neutrino oscillation tomography of the Earth's outer core are presented in Section 3. We start in Section 3.1 by quantifying the expected theoretical reach of the method under the hypothesis of perfect detector capabilities, showing how different assumptions for the outer core composition will indeed modify the number of neutrinos of different flavours interacting at a detector site. In Section 3.2 we move to investigating the realistic performances of the two main families of atmospheric neutrino detectors presently under construction, and discuss their ability to detect the presence of 1wt% Hydrogen in the outer core. Finally, we illustrate in Section 3.3 the evolution required for the next-generation of detectors to be able to discriminate FeNiH vs. FeNiSi<sub>x</sub>O<sub>y</sub> models of the Earth's core. The context and implications of our findings are further discussed in Section 4.

## 2 Theoretical background and methods

### 2.1 Neutrino oscillations in matter

Neutrino flavor oscillations are a quantum-mechanical phenomenon that arises because the neutrino flavor eigenstates  $\nu_e, \nu_\mu, \nu_\tau$ —which take part in weak interactions and are therefore the observable states—are not identical to the neutrino mass eigenstates  $\nu_1, \nu_2, \nu_3$ —which describe their propagation in vacuum. The flavor eigenstates are a quantum superposition of the mass eigenstates, whose relative phases change along the neutrino propagation path. This evolving mix of states leads to an oscillatory pattern of the

detection probability of a given neutrino flavor, which depends on the neutrino energy and traveled distance.

Neutrino oscillation probabilities are calculated by solving the Schrödinger equation  $i\partial_t|\nu(t)\rangle = H|\nu(t)\rangle$ . The neutrino propagation Hamiltonian  $H$  is approximated as the sum of two terms:

$$H = U \begin{pmatrix} 0 & 0 & 0 \\ 0 & \frac{\Delta m_{21}^2}{2E} & 0 \\ 0 & 0 & \frac{\Delta m_{31}^2}{2E} \end{pmatrix} U^\dagger + \begin{pmatrix} V_e & 0 & 0 \\ 0 & 0 & 0 \\ 0 & 0 & 0 \end{pmatrix}. \quad (3)$$

The first term represents intrinsic energy levels of the system in vacuum. Because neutrinos are generally observed in an ultra-relativistic context, the energy difference between mass states is approximately proportional to their difference in mass-squared  $\Delta m_{ij}^2 = (m_i^2 - m_j^2)$ . The Hamiltonian is shown in the flavor basis characterized by eigenstates of the weak interaction. The mixing matrix  $U$  represents the unitary transformation between the mass and flavor bases and is usually parametrized in terms of three mixing angles ( $\theta_{12}$ ,  $\theta_{13}$ ,  $\theta_{23}$ ) and a complex phase  $\delta$ , which are fundamental constants of physics [see, e.g., Giganti et al. (2018) for a general discussion of oscillation formulae].

The second term in Eq. 3 arises from coherent interactions of neutrinos with electrons in the medium in which they propagate (Wolfenstein, 1978; Mikheyev and Smirnov, 1985). The effective potential  $V_e = \pm\sqrt{2}G_F n_e$  induces a change in the electron flavor energy level that is directly proportional to the electron number density  $n_e$  and the Fermi constant  $G_F$ , which characterizes the strength of the weak interaction. The sign of the matter potential is positive for neutrinos and negative for antineutrinos.

The solution of the Schrödinger equation for such a system in matter of constant density amounts to computing the eigensystem of the full Hamiltonian. While in vacuum the eigenvalues and eigenvectors are given by  $\Delta m_{ij}^2/2E$  and the matrix  $U$  directly, the matter potential leads to effective eigenvalues and eigenvectors that depend on the electron density. This process can be interpreted as a modification of the fundamental parameters  $\Delta m_{ij}^2$  and  $\theta_{ij}$  induced by the neutrino environment.

For example, the effective mixing angle  $\tilde{\theta}_{13}$  and the effective mass-squared splitting  $\Delta\tilde{m}_{31}^2$  in matter are related to the corresponding parameters in vacuum *via*<sup>1</sup>:

$$\Delta\tilde{m}_{31}^2 \approx \xi \cdot \Delta m_{31}^2, \quad \sin^2 2\tilde{\theta}_{13} \approx \frac{\sin^2 2\theta_{13}}{\xi^2}, \quad (4)$$

with a mapping parameter

$$\xi = \sqrt{\sin^2 2\theta_{13} + \left( \cos 2\theta_{13} - \frac{2EV_e}{\Delta m_{31}^2} \right)^2}, \quad (5)$$

At the energy and distance scales relevant to atmospheric neutrino oscillations, the probability of observing a transition

between  $\nu_e$  and  $\nu_\mu$  flavors is proportional to  $\sin^2 2\theta_{13}$ , which is small in vacuum, as observed in oscillation measurements of reactor antineutrinos (Abe et al., 2012; Ahn et al., 2012; An et al., 2012) that are insensitive to the matter potential. However, the  $\nu_e \leftrightarrow \nu_\mu$  transition probability may become large or even maximal when  $\xi^2 \rightarrow \sin^2 2\theta_{13}$ , which translates into a resonance condition for the neutrino energy:

$$E \rightarrow \pm \frac{\Delta m_{31}^2 \cos 2\theta_{13}}{2\sqrt{2}G_F n_e}. \quad (6)$$

Neutrinos traversing the Earth will experience resonant oscillations in the outer core for energies  $\sim 3$  GeV, and in the mantle for  $\sim 7$  GeV, with the exact resonant energy depending on the electron density of the material.

## 2.2 Atmospheric neutrino propagation through the earth

An almost isotropic neutrino flux is constantly produced by the interaction of cosmic rays with air molecules, mainly coming from the decays of charged mesons ( $\pi^\pm$ 's and  $K^\pm$ 's) and muons. At energies above 100 Megaelectron Volts (MeV) approximately, these atmospheric neutrinos become the dominant neutrino flux observed on Earth. It occurs noting here that such energies are well above the ones ( $\sim$  few MeVs) typically attained by geoneutrinos, the electron (anti-)neutrinos produced in nuclear decays of radioactive elements like  $^{238}\text{U}$ ,  $^{232}\text{Th}$  and  $^{40}\text{K}$ , which are responsible for the Earth's radiogenic heat flux (Smirnov, 2019). While geoneutrinos have their own intrinsic interest for inferring information about the Earth's composition, they can be safely ignored in the present study which focuses on neutrinos with energies of 1 Gigaelectron Volt ( $10^3$  MeV) and above.

Atmospheric neutrino flux calculations rely on 3D Monte-Carlo simulations of air shower development, starting with a primary cosmic ray flux based on measurements, and including solar modulation, geomagnetic field effects and seasonal variations of the atmosphere density. For the present study, we use as input the flux produced by Honda et al. (2015) for the Gran Sasso site (without mountain over the detector), averaged over all azimuth angles and over seasonal variations, and assuming minimum solar activity. The flux is dominated by muon- and electron-(anti)neutrino components, with an approximate ratio of 2:1 between  $\nu_\mu$  and  $\nu_e$  flavors, and we have neglected the small contribution of  $\nu_\tau/\bar{\nu}_\tau$ .

For a given zenith angle of incidence  $\theta_z$ , as defined in Figure 1A, the neutrino trajectory across the Earth is modelled along the corresponding baseline through a sequence of steps of constant electron density which are inferred from a radial model of the Earth with 42 concentric shells of constant  $n_e$ , where mass density values are fixed and follow PREM. These shells are grouped into three petrological layers (inner core, outer core, and mantle+crust), whose composition, hence Z/A factor, is assumed to be uniform and provided in Table 1). In each shell, the electron density is determined from the mass density and Z/A according to Eq. 2. The probabilities of neutrino flavor transitions along their path through

<sup>1</sup> These expressions retain only the dominant term of a series expansion, assuming  $\Delta m_{21}^2/\Delta m_{31}^2 \ll 1$  and  $\theta_{13} \ll 1$ , in agreement with the measured values (Freund, 2001).

**TABLE 1** Compositional layers in the benchmark Earth model used in the analysis when assuming a pure FeNi outer core. The columns indicate the number of constant density shells (each of them taking its value from PREM), the exact innermost and outermost radius (in km) and the assumed Z/A value.

Layer	Shells	$[R_-, R_+]$	Z/A
Inner core	7	0–1,221.5	0.466
Outer core	12	1,221.5–3,480.0	0.466
Mantle + crust	23	3,480.0–6,368.0	0.496

the Earth are computed using the *OscProb*<sup>2</sup> package. The values of the parameters that enter the oscillation probability computation are taken from the global fit of neutrino data performed with the NuFIT analysis Version 5.0 (Esteban et al., 2020). We have assumed normal ordering of the neutrino mass states, *i.e.*,  $m_3 > m_1$ , which is currently favoured by NuFIT and other global fits of neutrino data (Capozzi et al., 2021; de Salas et al., 2021).

### 2.3 Determination of the rate of interacting neutrinos

Neutrinos with energies in the range ~1–100 GeV interact with matter mostly *via* scattering off nuclei, by exchanging either a neutral ( $Z^0$ ) or a charged ( $W^\pm$ ) weak-force boson that triggers a hadronic cascade. In neutral-current (NC) interactions, the neutrino survives in the scattering products and escapes. In charged-current (CC) interactions, the neutrino gives rise to a charged lepton counterpart of the same flavor ( $e$ ,  $\mu$ , or  $\tau$ ). While electrons immediately induce a secondary short electromagnetic cascade, muons travel relatively long distances, depending on their energy, before they are stopped. Because of the high mass of the  $\tau$  lepton ( $\approx 1.7$  GeV), the contribution of (anti-) $\nu_\tau$ -induced CC events is small in the range of energies relevant for tomography studies. For completeness, this flavor is nevertheless included in our computations.

The rate of neutrinos interacting in a given volume of target matter is then computed, for each interaction channel  $\alpha$  (NC/CC;  $e, \mu, \tau; \nu/\bar{\nu}$ ), as:

$$R_\alpha^{\text{int}}(E, \theta_z) \equiv \frac{d^4 N_\alpha^{\text{int}}(E, \theta_z)}{dE d\theta_z dt dM} = \left( \sum_{\beta=e,\mu} \frac{d^2 \Phi_{\nu_\beta}}{dE d\theta_z}(E, \theta_z) \cdot P_{\nu_\beta \rightarrow \nu_\alpha}(E, \theta_z) \right) \cdot \frac{\sigma_{\nu_\alpha}^{\text{int}}(E)}{m_N}, \quad (7)$$

where we have made explicit the dependence on the neutrino energy  $E$  and on the incoming zenith angle  $\theta_z$ , as defined in Figure 1A, under the assumption of a spherically symmetric mass density profile of the Earth. The angle  $\theta_z$  is directly related to the path length  $L$  through the Earth:  $L \approx -2R_\oplus \cos \theta_z$  with  $R_\oplus$  the radius of the Earth.

$R_\alpha^{\text{int}}(E, \theta_z)$  represents the differential rate of  $\nu_\alpha$  interactions (with target nucleons of mass  $m_N$ ) at the detector location, as a function

the energy and zenith angle and per unit exposure (defined as the product of running time and target mass of the detector). It is obtained as a product of the incident (differential) fluxes of atmospheric neutrinos  $\Phi_\beta$  (with  $\beta = e, \mu$  as the atmospheric  $\nu_\tau$  component is negligible), the flavor oscillation probability along each neutrino path  $P_{\nu_\beta \rightarrow \nu_\alpha}$ , and the neutrino-nucleon cross-section  $\sigma_{\nu_\alpha}^{\text{int}}$ , that quantifies the probability for a neutrino to interact (hence to generate a potentially detectable signal). A quantitative example is shown in Figure 1B, illustrating both the oscillatory effects and the attenuation of the flux at high energies, which is due to the energy power spectrum  $\propto E^{-3}$  of the cosmic ray flux that produce the neutrinos in the atmosphere (Honda et al., 2015).

### 2.4 Detector modelling

Neutrinos are observed only indirectly, through the signal deposited in the detector by the byproducts of their interaction. The ability to detect, reconstruct and identify the different types of neutrino events in the energy range of interest for Earth tomography is essentially driven by the detector size, technology and density of sensors. We consider here two main experimental approaches that are currently pursued for the upcoming generation of detectors targeting neutrinos with energies at the GeV scale, and that rely on different detection materials and observation strategies:

- Liquid Argon (LAr) detectors are a type of Time Projection Chamber (TPC) (Rubbia, 1977) that detects the electrons released upon ionization of Argon atoms along the paths of the secondary charged particles emerging from the neutrino interaction.
- Water-Cherenkov (wC) detectors instrument large volumes of water (or ice) with arrays of photosensors that detect the Cherenkov light induced by the secondary charged particles traveling faster than light in water (Tamm and Frank, 1937; Čerenkov, 1937).

LAr TPCs are able to reconstruct highly detailed 3D images of the neutrino event, providing excellent flavor identification capabilities, even at low (sub-GeV) energies, and energy and angular resolutions typically superior to water-Cherenkov detectors. The size of these detectors is however limited by their much higher cost. The first large-scale LArTPC detector was the ICARUS T600 detector (Rubbia et al., 2011), with an active mass of 476 tons. A new generation of LArTPCs is being developed for the DUNE experiment (Abi et al., 2020c), that will include four detectors of 10 kton active mass each.

The performance of water-Cherenkov detectors, on the other hand, is typically a trade-off between the target volume for neutrino interactions and the density of photosensors that sample the Cherenkov signal emitted by charged byproducts of the neutrino interaction. The Hyper-Kamiokande experiment (Abe et al., 2018) will consist in two ~200-kton water tanks overlooked by a dense array of photosensors covering its internal walls, providing a sub-GeV threshold for neutrino detection and excellent discrimination between electron-like and muon-like signatures. To access even larger target volumes, the ORCA (Adrian-Martinez et al., 2016;

2 J. Coelho et al., <https://github.com/joaobcoelho/OscProb>.

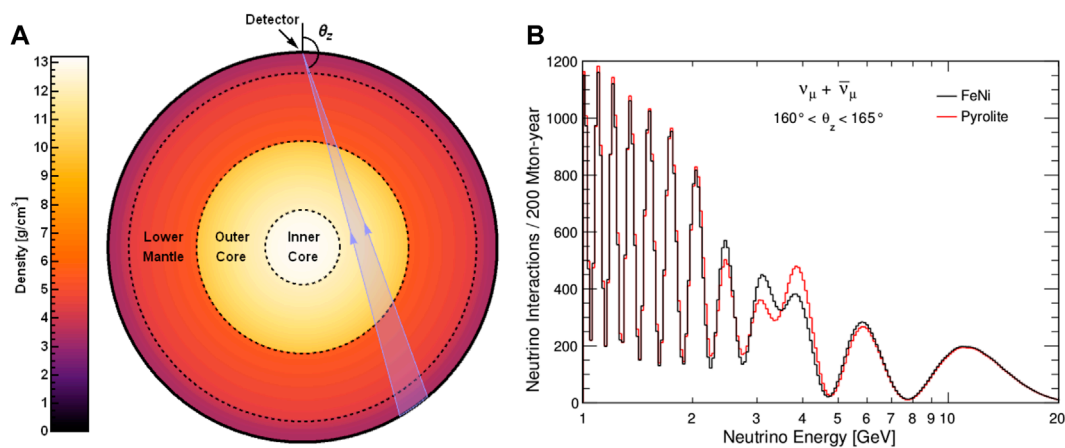


**FIGURE 1**

Oscillations of Earth-crossing neutrinos. **(A)**: A detector located at the surface will receive atmospheric neutrinos having traversed the Earth along different paths, as measured by their zenith angle  $\theta_z$  with respect to the vertical at the detector location. As these neutrinos cross the Earth, the amplitude of their oscillations at different depths will be affected by the local density of electrons. A modification in the electron density of the outer core would then affect the flavor mix of neutrinos that cross it. **(B)**: To illustrate this effect, the number of interactions expected for atmospheric muon neutrinos and antineutrinos ( $\nu_\mu + \bar{\nu}_\mu$ ) is shown as a function of the neutrino energy in a detector with 200 Mton-years exposure, assuming two extreme chemical compositions chosen for the sake of the argument, corresponding respectively to pure FeNi (a light-element-free outer core) and to pyrolite (same as the mantle). Only neutrinos expected from the angular region  $\theta_z \in [160^\circ, 165^\circ]$  highlighted on Panel (a), with a large intersection with the outer core, are shown. The observed oscillation pattern reflects a combination of disappearing ( $\nu_\mu \rightarrow \nu_e, \nu_\tau$ ) and appearing ( $\nu_e \rightarrow \nu_\mu$ ) muon-neutrinos. Differences related to the outer core composition model are most visible for neutrino energies between 2 and 5 GeV.

Aiello et al., 2022) and PINGU (Aartsen et al., 2017) experiments propose to instrument several Mtons of seawater or polar ice with a much sparser tridimensional array of photosensors. The gain in statistics comes at the expense of a higher detection threshold (few GeV) and worse energy and direction reconstruction capabilities, which also limit their performances for neutrino flavor identification. Water-Cherenkov detectors also cannot distinguish in first approximation between neutrino and anti-neutrino events.

To simulate the detector response, we use a set of parametrized analytical functions modeling the main performance features relevant for the detection, reconstruction and classification of neutrino events:

- The **effective mass**  $M_{\text{eff}}(E)$  is the product of the instrumented target mass  $M$  of the detector and its detection efficiency, i.e., the probability for a neutrino interaction to be successfully detected as an event.  $M_{\text{eff}}$  typically increases with the neutrino energy, until reaching a plateau that saturates the fiducial mass of the detector. We have conservatively neglected here a potential increase in  $M_{\text{eff}}$  for  $\nu_\mu$  CC events at high energies, corresponding to through-going muons created in neutrino interactions outside of the detector target volume. The threshold for detection is mainly driven by the density (and intrinsic efficiency) of sensors. We approximate  $M_{\text{eff}}(E)$  by a sigmoid function of  $\log(E)$  with two adjustable parameters  $E_{th}$  and  $E_{pl}$ , which correspond to energies where the detection efficiency reaches 5% and 95% respectively.
- The **energy resolution** parameterizes the relative error on the reconstructed neutrino energy in the form of a

Gaussian probability distribution function (p.d.f.) with energy-dependent width:  $\sigma_E(E)/E = A_E + B_E/\sqrt{E}$ .

- The **angular resolution** parameterizes the error on the measured zenith angle in the form of a von Mises-Fisher p.d.f. on a sphere marginalized with respect to azimuth. For wC detectors we take into account the dependence of  $\sigma_\theta$  on the energy as  $\sigma_\theta(E) = A_\theta + B_\theta\sqrt{E}$ .
- The **classification efficiency**  $\varepsilon_{\text{class}}(E)$  describes the probability for a neutrino event of energy  $E$  to be correctly classified into one of the topological channels observable by the detector. We model it with a sigmoid as a function of  $\log(E)$  with adjustable threshold ( $E_{th}^{\text{class}}$ ) and plateau ( $E_{pl}^{\text{class}}$ ) energies, maximal identification probability  $P_{\text{max}}^{\text{class}}$  and minimum probability of 50% (corresponding to the case of no separation power).

Events are classified according to their topological features, which depend on the signature of each interaction channel (NC/CC;  $e/\mu/\tau$ ;  $\nu/\bar{\nu}$ ). In practice, the relative sparseness of instrumentation limits the signal sampling in the detector, and thus the reconstruction and identification performances.

In this study we assume that all detectors under consideration have the basic capability to classify events into two main observational classes: *track*-like events, which are mostly associated to  $\nu_\mu$  charged-current interactions producing a long muon track, and *cascade*-like events, when there is no such single muon or the muon energy is too small for it to be distinguished among the many other secondary particles created in the event. The *cascade* channel therefore comprises mainly  $\nu_e$  CC and

(subdominantly)  $\nu_\tau$  CC interactions, plus a small contribution from  $\nu_\mu$  CC interactions without an observable muon, and all NC interactions.

For NC interactions, a fraction of the energy of the event is carried away by an invisible outgoing neutrino, resulting in a lower reconstructed energy and degraded angular resolution. Because NC-induced events are blind to neutrino flavor, they only decrease the experiment sensitivity. Fine-grained detectors like DUNE and Hyper-Kamiokande have some capability to separate and reject the NC-induced events from the  $\nu_e$  CC events, thereby increasing the flavor purity of the cascade channel. To account for a possible related improvement in the detector sensitivity, we have considered here both the baseline case that includes the NC-induced events in the cascade sample, and the optimistic case where the NC-induced contributions are completely removed from the sample. We have also used throughout our study the neutrino-nucleon cross-sections weighted for water molecules obtained with the GENIE Monte Carlo neutrino generator (Andreopoulos et al., 2010), neglecting the small difference in cross-section for interactions on Argon nuclei in the case of the DUNE detector.

## 2.5 Computation of the expected signal

In order to obtain the expected signal in a realistic experiment, the rate of interacting neutrinos as obtained from Eq. 7 must be weighted with the appropriate detection efficiency at each incoming neutrino energy. In the following we use the subscript “true” for the quantities (energy and zenith angle) that refer to the incoming neutrino properties, and “reco” for their reconstructed values as provided by a given detector. The observed event rate is computed by a discretized convolution of the interacting rate at energy  $E_{\text{true}}$  and incident at zenith angle  $\theta_{\text{true}}$  over the E-cos  $\theta$  plane according to the energy and zenith resolution p.d.f.s. The reconstructed events for each interaction channel are distributed into the two observational channels (*tracks* and *casades*) according to the classification efficiency function  $\varepsilon_{\text{class}}(E)$ . Every bin in the final  $(E_{\text{reco}}, \theta_{\text{reco}})$  event oscillogram therefore (i) contains a certain fraction of misreconstructed events coming from other  $(E_{\text{true}}, \theta_{\text{true}})$  bins; and (ii) misses some events that end up misreconstructed into different  $(E_{\text{reco}}, \theta_{\text{reco}})$  bins.

The final event rate expected in a given channel, in a given bin of reconstructed energy and zenith angle, is thus obtained as follows for the *track* channel:

$$R_{\text{tracks}}^{\text{obs}}(E_{\text{reco}}, \theta_{\text{reco}}) = \sum_{E_{\text{true}}, \theta_{\text{true}}} \left[ R_{\text{tracks}}^{\text{int}}(E_{\text{true}}, \theta_{\text{true}}) \varepsilon_{\text{class}}(E_{\text{true}}) + R_{\text{casc}}^{\text{int}}(E_{\text{true}}, \theta_{\text{true}}) (1 - \varepsilon_{\text{class}}(E_{\text{true}})) \right] \times PDF_{\text{angle}}(\theta_{\text{reco}}; E_{\text{true}}, \theta_{\text{true}}) \times PDF_{\text{energy}}(E_{\text{reco}}; E_{\text{true}}) \times \Delta E_{\text{true}} \times \Delta \theta_{\text{true}} \times M_{\text{eff}}(E_{\text{true}}), \quad (8)$$

where  $PDF_{\text{angle}}$  and  $PDF_{\text{energy}}$  represent the probability distribution functions of the angular and energy resolutions as defined above. A similar expression can be straightforwardly derived for the event rate in the *cascade* channel.

Independently of any classical measurement error, the intrinsically probabilistic nature of neutrino interactions as a quantum process induces a statistical uncertainty on the number of events observed in each bin of  $(E_{\text{reco}}, \theta_{\text{reco}})$ . Our statistical analysis is based on the standard Asimov dataset approach, in which all observed quantities are set equal to their expected values. The probability to detect  $N$  neutrino events of a given topology, e.g., *tracks*, in a predetermined interval of reconstructed energy and zenith angle is distributed according to a Poisson law, parametrized by the expected number of events  $N_{\text{exp}} = R_{\text{tracks}}^{\text{obs}}(E_{\text{reco}}, \theta_{\text{reco}}) \times T$ , where  $T$  corresponds to the duration of data taking. The observed number  $N$  will randomly deviate from this expectation with a relative standard deviation  $\sigma(N)/N_{\text{exp}} = 1/\sqrt{N_{\text{exp}}}$ . This uncertainty on the final measurement can only be mitigated by increasing the size of the event sample, which is proportional to the detector exposure.

Once these fluctuations are taken into account, we compute the log-likelihood ratio  $\lambda_{LLR}$  of the resulting event histograms, which yields a measure of the significance to reject model B (the “test hypothesis”) if model A (the “null hypothesis”) is true. According to Wilk’s theorem, for large enough statistics, the Poisson-distributed events converge towards a normal distribution, so that  $-2\lambda_{LLR}$  can be approximated by:

$$-2\lambda_{LLR} \approx \Delta\chi_i^2 = \frac{(n_A^i - n_B^i)^2}{n_A^i}. \quad (9)$$

The total  $\Delta\chi^2$  (integrated over all bins of energy and zenith angle) is related to the significance  $\sigma = \sqrt{\Delta\chi^2}$ , that gives the confidence level (C.L.) by which the test hypothesis can be excluded under the assumption of the null hypothesis. We have checked that the main conditions for Wilk’s theorem to apply were satisfied in our case: namely, that the simulated statistical sample was large enough, and that the sampled interval of  $Z/A$  was sufficiently far away from its boundary values (0 and 1).

## 3 Results

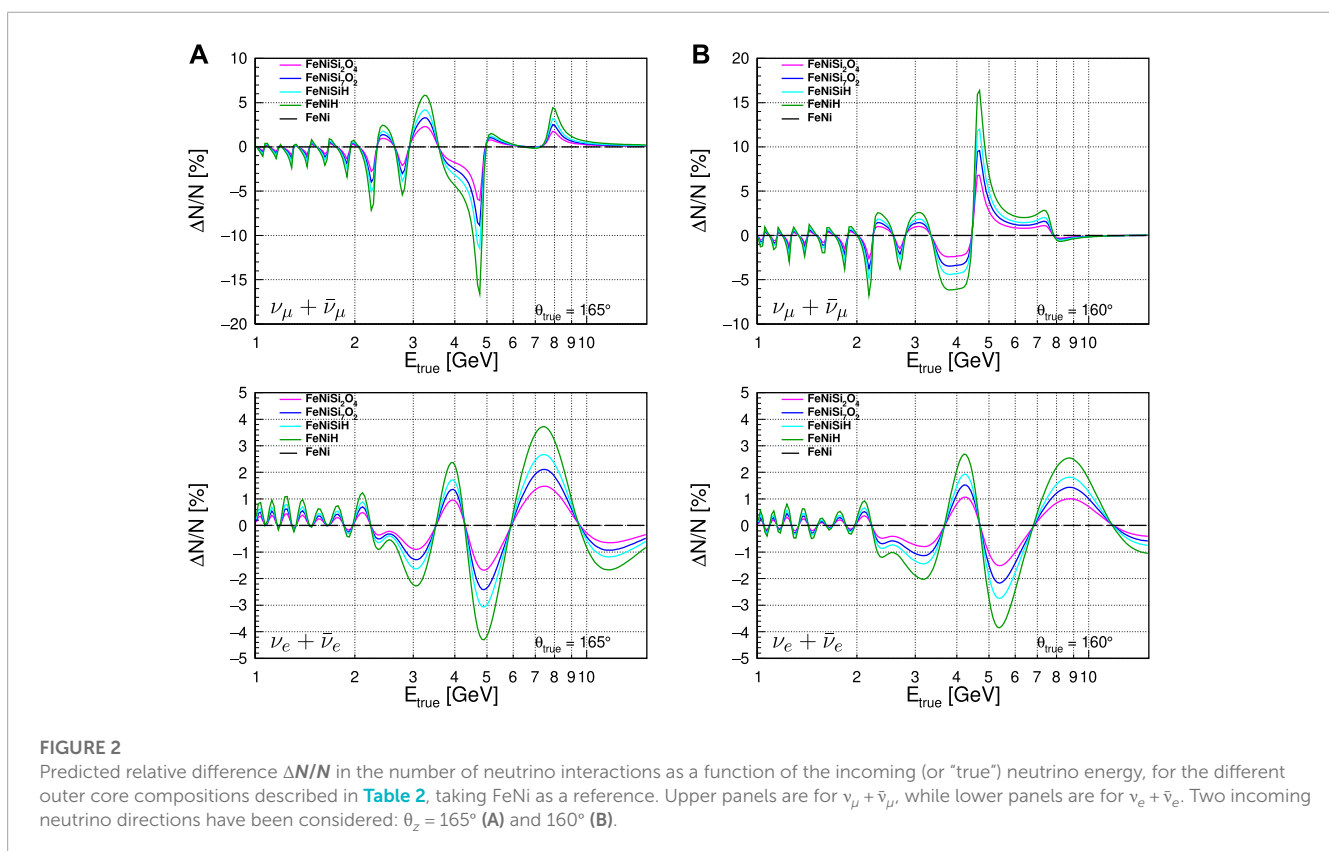
### 3.1 Theoretical reach

Based on the simulation chain described in Section 2, our first step is to evaluate the intrinsic sensitivity of the method by conducting detailed computations of the propagation of neutrinos through the Earth and comparing the expected rate of interacting neutrino events in a perfect detector under different assumptions for the outer core composition.

From Eq. 7, one can generate the two-dimensional (2D) distributions of expected number of neutrino interactions of a given flavor as a function of  $(E, \theta_z)$ , or *oscillograms*, for any specific exposure of a perfect detector that would observe atmospheric neutrinos from all directions. Because of the dependence of neutrino oscillation on  $n_e$  along the neutrino path, changes in the outer core composition (i.e., different  $Z/A$ ) induce variations in the expected signal, depending on the neutrino energy and exact trajectory (or equivalently,  $\theta_z$ ), that get imprinted in the oscillograms.

**TABLE 2** Models of outer core composition considered in this study, showing the weight fraction of the different elements and corresponding average  $Z/A$ . The FeNi model is the benchmark alloy used to model the inner core composition, whereas other models introduce different combinations of light elements: FeNiSi<sub>2</sub>O<sub>4</sub> (Badro et al., 2015), FeNiSi<sub>2</sub>O<sub>2</sub> (Kaminski and Javoy, 2013), FeNiSiH (Tagawa et al., 2016) and FeNiH (Sakamaki et al., 2016). In all models the Ni content is set to 5 wt% and Fe is the complement to 100% once light elements have been taken into account. All elements in the table have a  $Z/A$  ranging between 0.46 and 0.50, except Hydrogen whose  $Z/A = 1$  is responsible for pulling the average  $Z/A$  to higher values.

Label	FeNi	FeNiSi <sub>2</sub> O <sub>4</sub>	FeNiSi <sub>2</sub> O <sub>2</sub>	FeNiSiH	FeNiH
Composition	95 wt% Fe	89 wt% Fe	86 wt% Fe	88.2 wt% Fe	94 wt% Fe
	5 wt% Ni	5 wt% Ni	5 wt% Ni	5 wt% Ni	5 wt% Ni
	-	2 wt% Si	7 wt% Si	6.5 wt% Si	1 wt% H
	-	4 wt% O	2 wt% O	0.3 wt% H	-
$Z/A$	0.4661	0.4682	0.4691	0.4699	0.4714



We have quantified this effect by computing the relative difference ( $\Delta N/N$ ) in expected number of neutrino events between oscillograms generated with different models of outer core composition. We considered five different models (see **Table 2**), ranging from a pure FeNi alloy to a Hydrogen-rich (FeNiH) one, with two intermediate models chosen from the FeNiSi<sub>x</sub>O<sub>y</sub> family. As mentioned in the introduction, silicon and oxygen are not the only light elements that have been proposed in conventional models of the outer core; also sulphur and carbon could be present (Poirier, 1994), but their  $Z/A$  is too close to that of Si and O to allow for a discrimination by means of this method. Furthermore, high-pressure/high-temperature thermodynamics modelling appear to rule out Fe-Si-C compositions (Huang et al.,

2022). Therefore we do not consider them further in this study.

**Figure 2** illustrates the expected impact of the composition in terms of  $\Delta N/N$  for muon- and electron-neutrino interactions, as a function of the neutrino energy, for two different incoming directions. The predicted numbers of interactions for those particular configurations are shown to differ by up to 4% for electron neutrinos, and up to 17% for muon neutrinos, depending on the core composition considered. Furthermore, because the shape of the signal changes a lot depending on the zenith angle, it appears important to consider the signal in two dimensions (i.e., as a function of  $E$  and  $\theta_z$ ). This is further illustrated in **Figure 3** showing the full 2D distributions of  $\Delta N/N$  for muon- and electron-neutrino

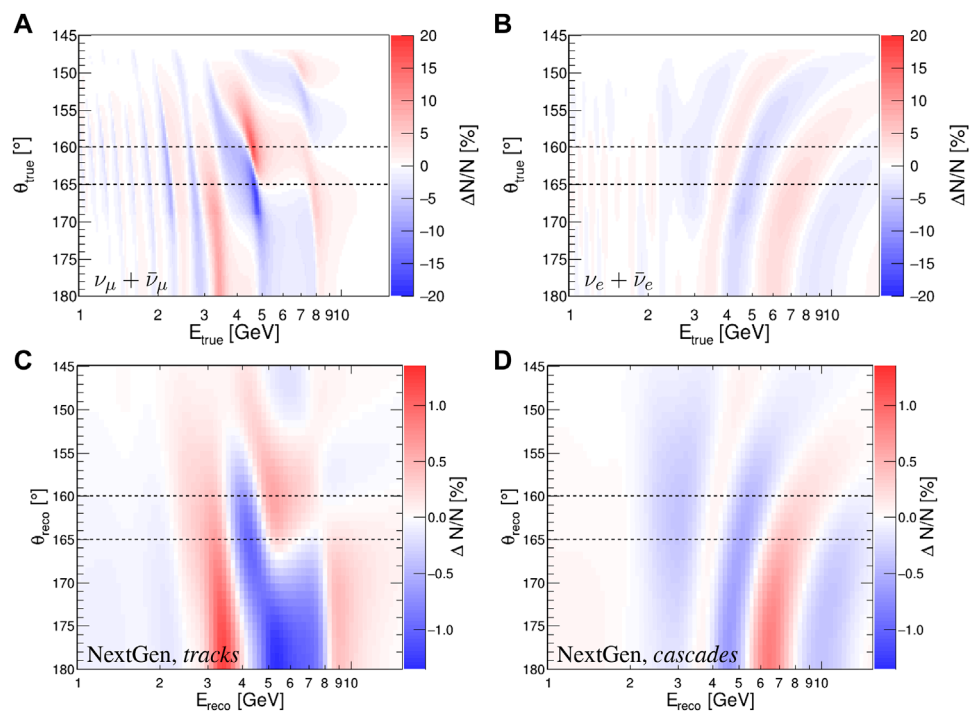


FIGURE 3

Upper panels: expected relative difference  $\Delta N/N$  in the number of neutrino interactions, as a function of the incoming (or “true”) neutrino energy and zenith angle, for the composition models FeNiH vs. FeNi. (A) panel is for  $\nu_\mu + \bar{\nu}_\mu$ , while (B) panel is for  $\nu_e + \bar{\nu}_e$ . The horizontal dashed lines correspond to the two incoming directions considered for the plots in Figure 2. Lower panels: expected relative difference  $\Delta N/N$  in the number of detected events, as a function of the reconstructed neutrino energy and zenith angle, for the composition models FeNiH vs. FeNi, for the Next-Generation (NextGen) detector described in Section 3.2 and Table 3. (C) panel is for the *track*-like events (mostly associated with  $\nu_\mu$  interactions) and (D) panel is for *cascade*-like events (mainly from  $\nu_e$  and  $\nu_\tau$  interactions), as defined in Section 2.4.

**TABLE 3** Inputs for the response functions of the detectors considered in this study (as discussed in Section 3.2): total target mass; threshold and plateau energy for the detection efficiency curve; energy and zenith resolutions; threshold and plateau energy for the classification efficiency curve; maximal classification probability achievable.

Detector	$M$ (Mton)	$E_{th}$ (GeV)	$E_{pl}$ (GeV)	$\sigma(E)/E$	$\sigma_\theta$ (deg)	$E_{th}^{class}$ (GeV)	$E_{pl}^{class}$ (GeV)	$p_{max}^{class}$
ORCA-like	8	2	10	25%	$30/\sqrt{E}$	2	10	85%
Hyper-Kamiokande-like	0.40	0.1	0.2	15%	$15/\sqrt{E}$	0.1	0.2	99%
DUNE-like	0.04	0.1	0.2	5%	5	0.1	0.2	99%
Next-Generation	10	0.5	1.0	$5\% + 10\%/\sqrt{E}$	$2 + 10/\sqrt{E}$	0.5	1	99%

interactions, for a specific comparison between FeNiH and FeNi core compositions. Such results confirm that a detailed study of the neutrino event rate in the energy range 1–10 GeV has the potential to constrain the Earth’s outer core composition.

### 3.2 Sensitivity of upcoming neutrino detectors to the outer core composition

The distributions shown in the upper panels of Figure 3 implicitly relate to a detector with 100% detection efficiency, perfect energy and  $\theta_z$  resolution, and infinite statistics. In reality, the measurement accuracy will be limited by experimental effects,

resulting in some blurring and attenuation of the signal, as illustrated in Figure 3 (lower panels). As discussed in Section 2.4, the detector technology and specifications (size, detection efficiency, resolution and particle identification) affect its ability to reconstruct the neutrino properties (energy, direction and flavor), and the intrinsically probabilistic nature of neutrino interactions induces a statistical uncertainty on the final observed number of events. The detector thus needs to be scalable to a sufficiently large volume for this uncertainty to be smaller than the intrinsic signal.

To investigate the influence of specific detector characteristics on their potential to constrain the core composition, we use the parametrized functions defined in Section 2.4 to model the key experimental features - namely, the effective mass, the direction and



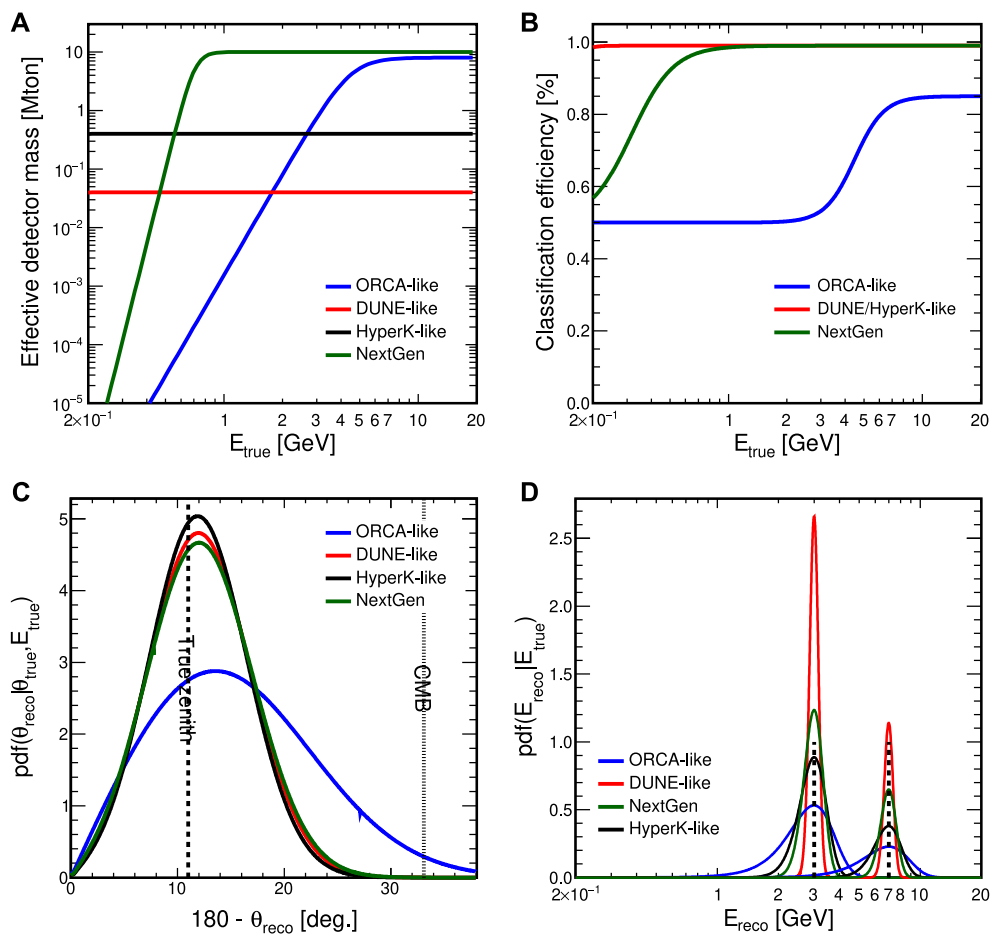


FIGURE 4

Examples of response functions used for the modelling of the neutrino detectors. (A): Effective detector mass ( $M_{\text{eff}}$ ) as a function of the neutrino true energy. (B): Classification efficiency ( $\rho_{\text{class}}$ ) as a function of the true neutrino energy. (C): Probability distribution function for the reconstructed zenith angle for a neutrino with true energy  $E_{\text{true}} = 10$  GeV and true zenith angle  $\theta_{\text{true}} \approx 169^\circ$  (corresponding to a neutrino trajectory grazing the inner-outer core boundary). (D): Probability distribution function for the reconstructed energy for two specific values of the true neutrino energy ( $E_{\text{true}} = 1$  and 5 GeV).

energy resolutions, and the efficiency in identifying the neutrino flavor based on the classification of events into *track* and *cascade* topologies. We consider here four benchmark parametrizations with specific inputs chosen as educated guesses for different detectors representative of the upcoming generation of GeV neutrino detectors: Hyper-Kamiokande, ORCA, and DUNE. The detail of the parameters used for each detector is provided in Table 3.

The DUNE-like model (Abi et al., 2020a; 2020c; Kelly et al., 2022) accounts for the superior resolution and reconstruction capabilities of the Liquid Argon detection technique, at the cost of a much smaller instrumented volume. At the other extreme, the ORCA-like model (Adrian-Martinez et al., 2016; Aiello et al., 2022) reflects the higher detection threshold and degraded reconstruction performances that result from a sparsely instrumented - although larger - volume. The Hyper-Kamiokande-like model (Abe et al., 2018) is a middle-way option combining a medium-size detector with a low detection threshold and good reconstruction and identification capabilities, in line with those already achieved with its predecessor Super-Kamiokande (Suzuki, 2019). Although some

of the detectors considered here may be sensitive to neutrinos below 1 GeV, we have conservatively limited our study to neutrinos with energy in the range [1,40] GeV, which encompasses most of the expected oscillation tomography signal. Some examples of the corresponding response functions are presented in Figure 4 for the energy range under consideration.

The corresponding modelling, and the physical parameters used for each specific detector, are described in Section 2.4 and Table 3. By folding the detector response with the expected rate of neutrino interactions given by Eq. 7, and summing over all relevant interaction types, we obtain the predicted rate of observable events of a given observational class,  $R_{\text{track}}^{\text{obs}}(E_{\text{reco}}, \theta_{\text{reco}})$  or  $R_{\text{cascade}}^{\text{obs}}(E_{\text{reco}}, \theta_{\text{reco}})$  in a given bin of neutrino reconstructed energy and zenith angle. By integrating these quantities over time and effective mass of the detector, we generate 2D histograms of the expected number of events as a function of  $E_{\text{reco}}$  and  $\theta_{\text{reco}}$ , for a given detector exposure. Such oscillograms are the cornerstone of our discussion of the detectors capability to constrain the Earth's core composition, as illustrated in the lower panels of Figure 3.

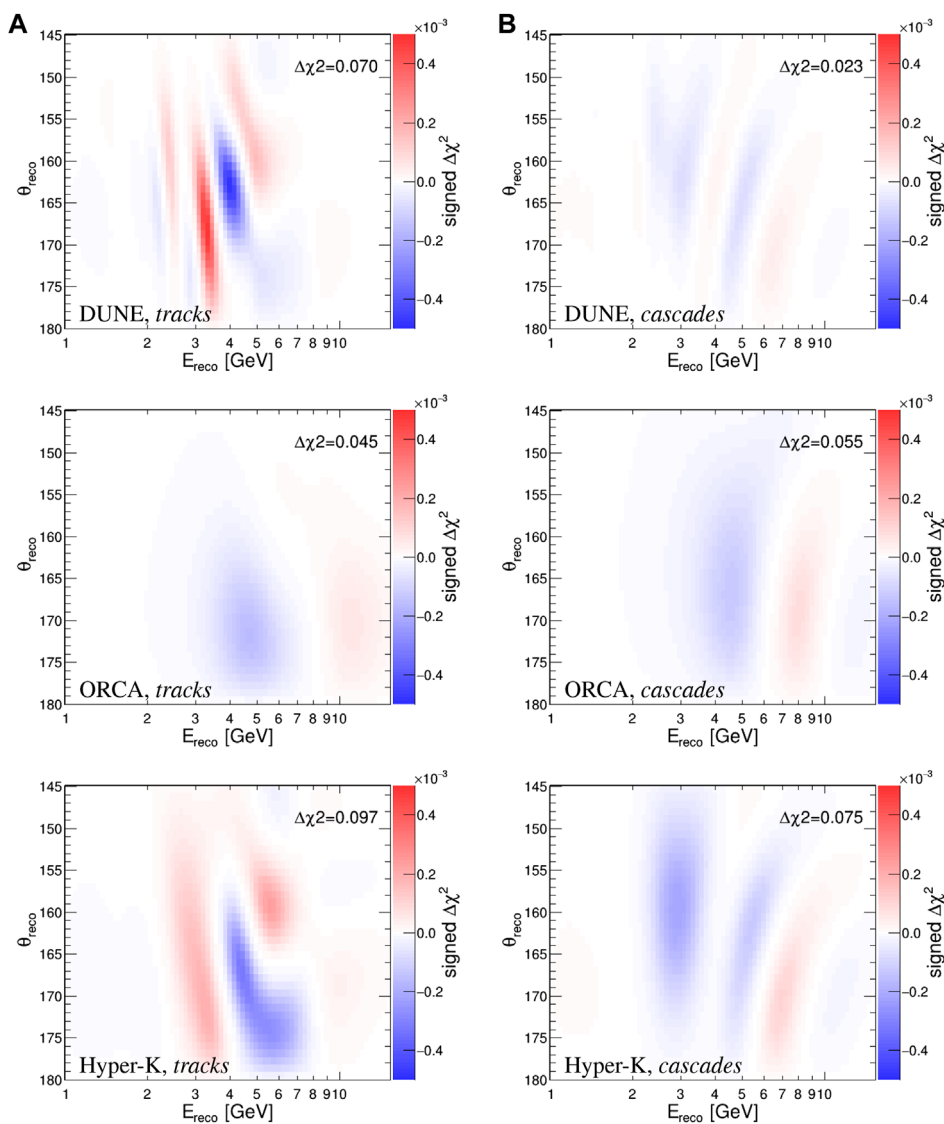


**FIGURE 5**

$\Delta\chi^2$  sensitivity for discriminating between FeNi model and FeNiH model in 20 years livetime of upcoming detectors. From top to bottom, the panels show the signed  $\Delta\chi^2$  maps (as defined in Section 2.5) as a function of the reconstructed neutrino energy and zenith angle, for DUNE, ORCA, and Hyper-Kamiokande, for *track*-like events (A) column and *cascade*-like events (B) column as defined in Section 2.4. The color scale is the same in all plots. The number indicated in each plot corresponds to the total  $\Delta\chi^2$  sensitivity summed (in absolute value) over all bins of the  $(E_{\text{reco}}, \theta_{\text{reco}})$  plane.

For a given detector, our projected experimental sensitivities are obtained from the detailed comparison of the full 2D oscillograms of expected neutrino events, generated with different assumptions for the core composition. As described in Section 2.5, a statistically meaningful way of quantifying the detector performance is to apply a  $\chi^2$  hypothesis test to the 2D histograms of expected events in bins of  $(E_{\text{reco}}, \theta_{\text{reco}})$ . Under the assumption of the validity of Wilk's theorem, the total  $\Delta\chi^2$  associated to a given pair of composition models, say A and B, is directly related to the significance  $\sigma = \sqrt{\Delta\chi^2}$ , giving the confidence level (C.L.) by which model A can be discriminated from model B. Examples of signed  $\Delta\chi^2$  maps for different upcoming detectors are presented in Figure 5 for the discrimination between FeNi and FeNiH models. The three detectors achieve a comparable statistical significance in the measurement of the outer core Z/A

after 20 years of data taking, although their sensitivity does not necessarily come from the same region of the  $(E, \theta)$  plane, nor from the same observational channel.

Figure 6 compares more directly the performances of the benchmark detectors in discriminating outer core composition models. Despite the differences in technology, size and reconstruction performances, we find that ORCA and DUNE reach a similar precision of 0.016 (at  $1\sigma$  C.L.) on the absolute Z/A measurement after 20 years of data taking. These results are comparable with the ones previously published (Bourret and Van Elewyck, 2019) based on a full simulation of the ORCA detector. They confirm the capability of these detectors to measure the Z/A in the Earth's outer core with a  $1\sigma$  relative precision of 3–4 percent. Hyper-Kamiokande performs slightly better, with

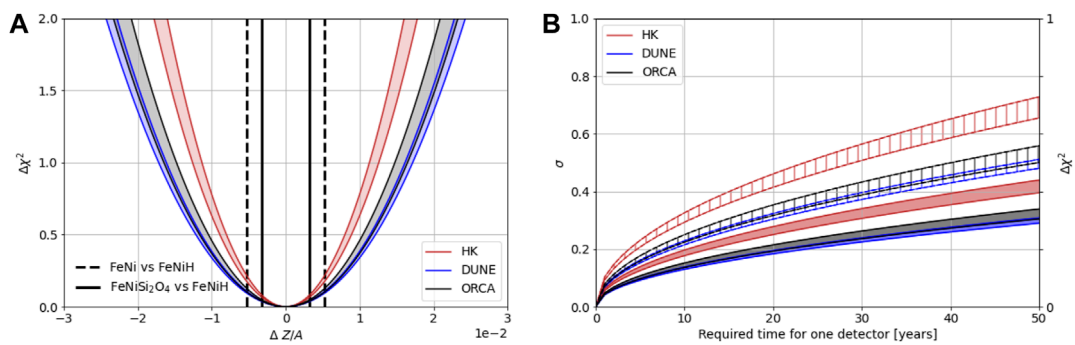


FIGURE 6

Sensitivity of the individual upcoming detectors to the outer core composition. (A) Sensitivity profile for the absolute precision in the  $Z/A$  measurement, for 20 years operation of the Hyper-Kamiokande, DUNE and ORCA detectors. The vertical lines indicate the  $Z/A$  separation between specific pairs of models of core composition. (B) Sensitivity bands as a function of the detector lifetime, for discriminating specific pairs of models. In the (B) plot, the filled bands represent the discrimination power between FeNiSi<sub>2</sub>O<sub>4</sub> and FeNiH, while the hashed bands represent FeNi vs. FeNiH. The band limits in both plots correspond to the baseline and optimistic assumptions on the detectors capability to filter out events which are insensitive to neutrino flavor (as explained in Section 2.4).

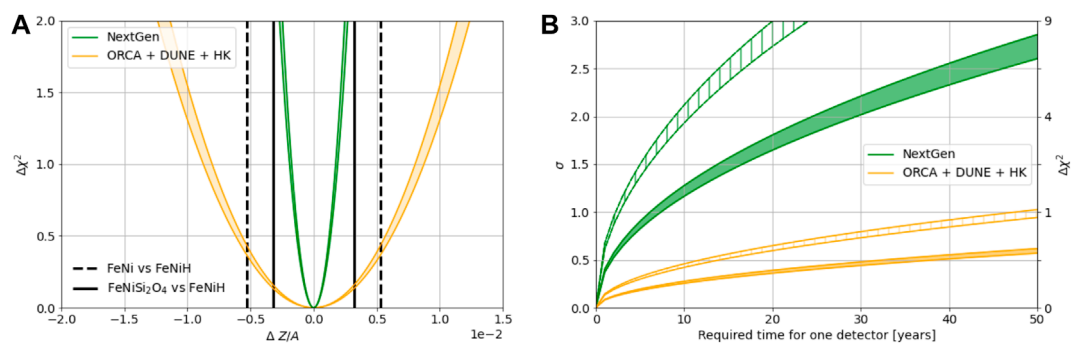


FIGURE 7

Sensitivity to the outer core composition for upcoming and next-generation detectors. (A)  $\Delta\chi^2$  profile for the absolute precision in the  $Z/A$  measurement, for 20 years operation of a Next-Generation (NextGen) detector and for the combination of DUNE, ORCA and Hyper-Kamiokande (HK) over the same lifetime. The vertical lines indicate the  $Z/A$  separation between specific pairs of models of core composition. (B) Sensitivity bands as a function of the detector lifetime, for discriminating specific pairs of models. In the (B) plot, the filled bands represent the discrimination power between FeNiSi<sub>2</sub>O<sub>4</sub> and FeNiH, while the hashed bands represent FeNi vs. FeNiH. The band limits correspond to the baseline and optimistic assumptions on the detectors capability to filter out events which are insensitive to neutrino flavor (as explained in Section 2.4).

a relative precision of 2.5%, yielding a discrimination power of approximately  $0.5\sigma$  between FeNi and FeNiH models for 25 years of measurements. A higher sensitivity can be achieved by combining the data from the three detectors into one single measurement; in that case, a  $1\sigma$  C.L. discrimination power for FeNiH vs. FeNi could be reached in 50 years of concomitant data taking, as can be seen in Figure 7.

### 3.3 A next-generation detector to identify the light elements in the outer core

While the previous result can be seen as a promising proof of concept of the method, achieving the next level of sensitivity requires both beating the statistical limitation by scaling up the detectors in size, and achieving excellent reconstruction performances (flavor,

$E_{\text{reco}}, \theta_{\text{reco}}$ ), in order to better resolve the patterns in the 2D  $(E_{\text{reco}}, \theta_{\text{reco}})$  event distributions.

Based on the results obtained for the upcoming detectors, we have investigated possible realizations of such a next-generation, or NextGen, detector, that would combine the best performances of current-generation instruments, taking as benchmarks a 1 GeV detection threshold and almost perfect (99%) discrimination between *track*-like and *cascade*-like events.

We performed a systematic scan of the discrimination potential of such detector over a large range of sizes, energy and angular resolutions, as presented in Figure 8. A separation power of at least  $1\sigma$  between FeNiSi<sub>2</sub>O<sub>4</sub> and FeNiH models can be obtained with a rather wide combination of zenith/energy resolution parameters. A good compromise is found in the region around  $\sigma(\theta) = 7^\circ$  angular resolution and  $\sigma(E)/E = 10\%$  energy resolution, not far from the performances associated with Hyper-Kamiokande, but

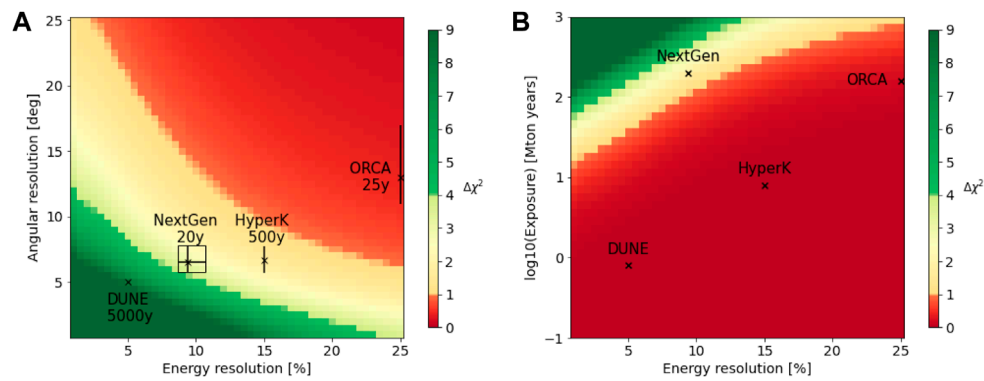


**FIGURE 8**

$\Delta\chi^2$  sensitivity for discriminating  $\text{FeNiSi}_2\text{O}_4$  vs.  $\text{FeNiH}$  with a NextGen detector for various combinations of exposure, energy and angular resolutions. The (A) plot is obtained for a fixed exposure of 200 Mton yr. The color scale indicates the intervals between 1, 2, and 3  $\sigma$  (68%, 95%, 99% C.L.). Superimposed on the maps are the lifetimes required to reach the 200 Mton yr exposure for DUNE, ORCA and HK detectors, as well as their specific resolution in the energy range of interest for the tomography measurement (3–7 GeV). The (B) plot is obtained by assuming a linear relationship between the energy and angular resolutions for the benchmark detectors, as suggested by the (A) plot.

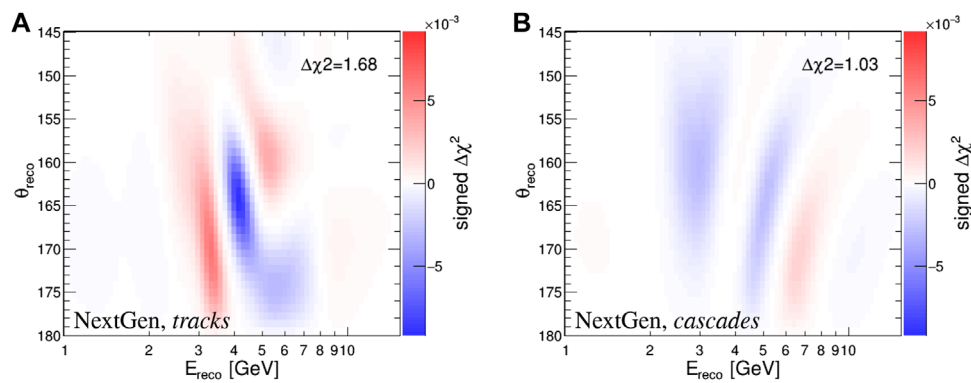


**FIGURE 9**

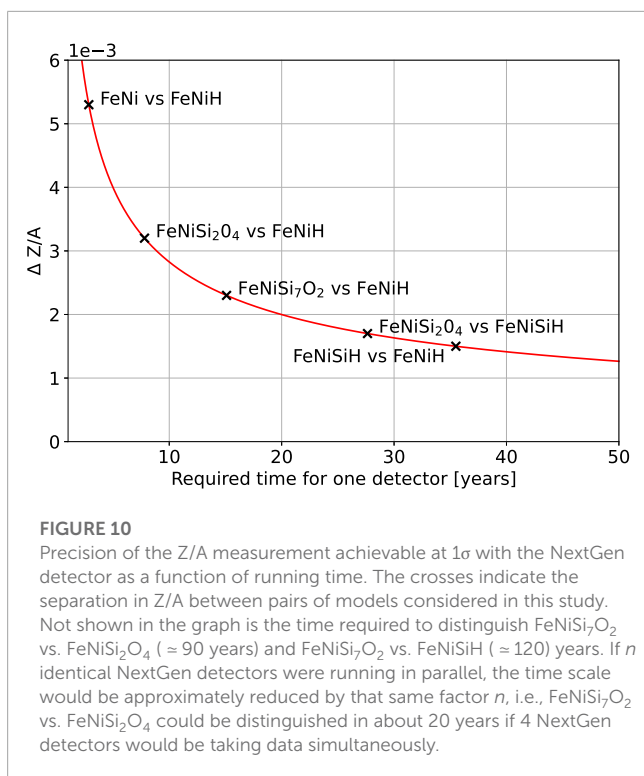
Sensitivity of the NextGen detector for discriminating between  $\text{FeNiSi}_2\text{O}_4$  and  $\text{FeNiH}$  outer core compositions after 20 years data taking. The plots show the signed  $\Delta\chi^2$  maps (as defined in Eq. 9) as a function of the reconstructed energy and zenith of the neutrinos, respectively for *track*-like (A) and *cascade*-like (B) events.

for a significantly larger, 10-Mton, detector. We provide a specific parametrization of such a NextGen detector in Table 3.

This scan also illustrates how the small size and limited scalability of Liquid Argon detectors is a serious obstacle to developing this technique to achieve the required exposure levels in a reasonable running time, despite their superior energy and zenith resolution. Even an asymptotic evolution of the DUNE experiment, with perfect identification of all neutrino flavors and interaction channels, would only reach a  $0.5\sigma$  discrimination power for  $\text{FeNiSi}_2\text{O}_4$  vs.  $\text{FeNiH}$  after 50 years running. We conclude that better perspectives for a core composition measurement arise from the water Cherenkov approach, provided that event reconstruction and identification performances similar or better to those of Hyper-Kamiokande can be achieved in a much larger (hence likely more sparsely instrumented) detector.

The performance of the NextGen detector is illustrated in Figure 9 in terms of the signed  $\Delta\chi^2$  maps for the discrimination between a  $\text{FeNiH}$  and a  $\text{FeNiSi}_2\text{O}_4$  composition of the outer core, for the *track* and *cascade* channels, for 20 years of data taking. In this example, the total  $\Delta\chi^2$  value is 2.71, respectively 1.68 for *track* and 1.03 for *cascade* channel.

The qualitative jump in performance that could be achieved with the NextGen detector is also evident in Figure 7 where its sensitivity is compared to the one obtained from combining ORCA, DUNE and Hyper-Kamiokande data. The characteristics of the NextGen detector yield a sub-percent precision on the Z/A measurement, sufficient to distinguish between  $\text{FeNiSi}_2\text{O}_4$  and  $\text{FeNiH}$  compositions at  $>1\sigma$  in a running time of about 10 years, well within the typical lifetime of a neutrino experiment (a discrimination at 90% C.L. would be achieved in about 20 years).



We further illustrate such capabilities in **Figure 10**, where we address the separability (at the  $1\sigma$  level) between pairs of realistic core composition models, as a function of the detector running time. Although a discrimination between composition models whose  $Z/A$  are closer than 0.001 (i.e.,  $\text{FeNiSi}_7\text{O}_2$  vs.  $\text{FeNiSi}_2\text{O}_4$ , or  $\text{FeNiSi}_2\text{O}_4$  vs.  $\text{FeNiSiH}$ ) appears out of reach, our results suggest that the NextGen detector would be able to exclude or confirm the FeNiH hypothesis against all the other realistic models considered in this study. This result can be obtained in less than 20 years if the actual outer core composition is in the family of models with an admixture of Silicon and Oxygen as only light elements.

## 4 Discussion

This paper presents a detailed study and comparison of the potential of upcoming atmospheric neutrino detectors to constrain the outer core composition to precision levels of relevance for geophysics. As a first step, we confirm the theoretical capability of neutrino oscillation tomography to discriminate between different realistic core composition models by computing the propagation and oscillation of atmospheric neutrinos through the Earth with well-established tools from the neutrino physics community. We note that the largest contribution to the theoretical signal is provided by atmospheric neutrinos reaching the detector in the  $\nu_\mu$  flavor, which may explain why many of the neutrino oscillation tomography studies to date have focused on this detection channel only.

The ultimate reach of this method, however, significantly depends on how the expected signal is effectively extracted in a

realistic experiment. In order to address this question in a flexible way and with a view to the future, we have developed our analysis based on analytical parametrizations of the detector response functions, similar in concept to the studies by [Winter \(2006\)](#) and [Rott et al. \(2015\)](#). This approach has allowed us to investigate for the first time different classes of experiments - namely, Liquid Argon TPCs and water-Cherenkov detectors - within a unified framework, based on educated guesses on the expected performances of the different detectors. Its implementation in terms of generic detection parameters would easily allow for further refinement in the description of the detector response to different observational channels, and also for comparisons with other neutrino detection techniques that could be proposed in the future. By making our code public, we aim at providing the community with a simple, versatile simulation tool to further explore the potential of neutrino oscillation tomography.

One notable conclusion to be drawn from our study, is that the respective contribution of the different neutrino flavours reaching the detector to the total signal (in terms of discrimination power for different core composition models) can vary significantly for different choices of the parametrized response functions, hence for different detectors, even within the same experimental approach. This observation emphasizes the importance of considering the neutrino signal in all its components - here, namely, the two observational channels *tracks* and *cascades*, in order to accurately assess the expected reach of a given experiment.

We have not addressed in detail in this study the more general question of systematic uncertainties related to the production, propagation (hence, oscillation) and interaction of atmospheric neutrinos, that may affect the accuracy of the  $Z/A$  measurement. The dominant sources of error on the neutrino fluxes come from uncertainties in hadron production along the atmospheric shower development, and subdominantly from uncertainties in the primary flux ([Barr et al., 2006](#)). The oscillation probabilities of neutrinos traversing the Earth depend on the squared mass differences  $\Delta m_{ij}^2$  of the neutrino mass eigenstates, and on the angles  $\theta_{ij}$  and complex phase  $\delta_{CP}$  that parametrize the mixing matrix  $U$  ( $i, j \in 1, 2, 3$ ). Some of these parameters have already been measured to a reasonable accuracy ( $O(5 - 15\%)$ ) by a variety of experiments using neutrinos from different sources (e.g., the Sun, the atmosphere, nuclear reactors, or man-made beams) ([Esteban et al., 2020](#)). The imperfect knowledge of  $\theta_{23}$ ,  $\Delta m_{31}^2$  and  $\delta_{CP}$ , which are currently the less constrained parameters, is most relevant for neutrino oscillations studies in the atmospheric domain.

The parameter having by far the largest impact on our results is the ordering of the neutrino mass eigenstates, and more specifically the (still unknown) sign of  $\Delta m_{31}^2$  which, according to Eq. 6, determines whether the matter-enhanced resonant oscillation happens for neutrinos or antineutrinos. After convoluting with the respective fluxes and cross-sections, the latter case (which corresponds to the inverted ordering with  $m_3 \ll m_1, m_2$ ) leads to a smaller statistics of interacting neutrino events, and also (more importantly) to a smaller effect in  $\Delta N/N$ . This results in a reduction of the sensitivity (in terms of  $\Delta\chi^2$ ) by a factor of about 7, hence of  $\sqrt{7}$  on the  $Z/A$  interval, independently of the detection performances. It equivalently translates into a factor of seven on the detector exposure needed to achieve the same

sensitivity level as in the normal ordering. This also motivates additional efforts to discriminate neutrinos from antineutrinos in the future generation of experiments - one possibility not discussed here being the use of a magnetized detector to identify the sign of the secondary lepton produced in the neutrino interaction (Kumar and Agarwalla, 2021). In any case, it is expected that the neutrino mass ordering will be measured with high confidence on a timescale of a decade (or less), either by the JUNO reactor neutrino experiment (An et al., 2016), by ORCA (Aiello et al., 2022) or by using man-made neutrino beams targeting the DUNE (Abi et al., 2020b) and Hyper-Kamiokande (Abe et al., 2015) detectors—JUNO having the advantage of being completely independent of matter effects<sup>3</sup>.

The impact of systematic uncertainties related to the oscillation parameters and to the normalization, shape and flavour content of the atmospheric neutrino flux have been discussed more extensively in some other recent studies, both for ORCA-like (Rott et al., 2015; Winter 2016; Bourret and Van Elewyck, 2019; Capozzi and Petcov, 2022; D'Olivo Saez et al., 2022) and DUNE-like (Kelly et al., 2022) detectors, and shown to have a limited to moderate impact on tomographic measurements. In the specific case of the measurement of the core composition which is our focus here, we benefit from the fact that such systematic effects can be mitigated and controlled by exploiting the sample of neutrino events that only traverse the mantle (and not the core). Moreover, the uncertainties on both the atmospheric neutrino fluxes and the oscillation parameters (in particular on  $\theta_{23}$ , which also has a significant impact on oscillation probabilities for atmospheric neutrinos at the GeV energy scale) will significantly reduce in the course of the upcoming decade, as a result of the current neutrino experimental program. Therefore those systematics should be much better constrained by the time the detectors discussed here have accumulated sufficient statistics to efficiently investigate the Earth's core composition.

Taking advantage of the versatility of our framework, we have further investigated the desirable detection performances for a NextGen detector that - contrarily to the upcoming generation of experiments - would be optimized for neutrino oscillation tomography. We find that such performances stem from two complementary aspects: (i) the large statistics of events provided by an experiment with 10 Mton target mass and a relatively low ( $\sim 1$  GeV) energy threshold that fully covers the energy range where resonant oscillation effects are expected for core-crossing neutrinos; and (ii) the state-of-the-art event reconstruction and classification capabilities. Limitations to this measurement arise from the intrinsic, quantum fluctuations in the particle content of the hadronic shower that results from the fragmentation of the nucleus hit by a neutrino. These effects have been extensively discussed for ORCA-like detectors (Adrián-Martínez et al., 2017) and shown to limit the performances as long as individual particles in the neutrino-induced cascades cannot be reconstructed. This limitation is mitigated in instrumented water tanks similar to Hyper-Kamiokande, thanks to the high density of sensors that allows

a sufficient sampling of the particles produced by the neutrino interaction.

In view of the above considerations, our favours go to the water-Cherenkov technique to define the path towards a Next-Generation detector able to reliably test the FeNiH hypothesis for the Earth's outer core composition. Such a detector should combine a multi-Megaton target volume with a sufficient density of sensors to achieve an efficient sampling of the neutrino event topology. Because of the limited scalability of man-made water tanks, we rather advocate for a hyperdense network of light sensors deployed in natural reservoirs of water or ice. The detector topology could be either three-dimensional (similar to ORCA) or two-dimensional (similar to Hyper-kamiokande) as long as it provides good angular coverage for neutrinos crossing the Earth's outer core. In this latter case, one possible configuration could consist in an immersed "carpet" of densely packed photosensors looking downwards, monitoring a large target volume of water or ice. The resulting loss in sensitivity to near-horizontal neutrinos (i.e.,  $\theta \sim 90^\circ$ ) should have minimal impact on the tomography measurement: all neutrinos crossing the core will reach the detector at an angle larger than  $57^\circ$  (corresponding to  $\theta_Z \geq 147^\circ$ ), and also a significant fraction of those traversing only the mantle will be detected and exploitable as a reference sample. Existing proposals for neutrino detectors made in different contexts, such as the hyper-dense 3D network Super-ORCA (Hofestädt et al., 2020) or the multi-megaton shallow-water network of steel tanks TITAND proposed for proton decay studies (Suzuki, 2001) might also be worth reevaluating in terms of their capabilities for neutrino oscillation tomography.

Finally, we emphasize that the timescale required for the measurements described here is inversely proportional to the total detection volume available. Deploying multiple detector units at different positions on the surface of the globe - an effort currently being achieved with sparse wC detectors focusing on high-energy neutrino astronomy - has the extra appeal to allow for a fully 3-dimensional analysis with potentially higher scientific reach. Such a network of detectors would not only be of great interest for Earth tomography purposes, but would also provide an unprecedented tool for high-statistics and high-precision studies of atmospheric neutrinos.

## Data availability statement

The datasets presented in this study can be found in online repositories. The names of the repository/repositories and accession number(s) can be found below: <https://gitlab.in2p3.fr/apc-tomography/earthprobe>.

## Author contributions

The idea was developed by EK and VVE and the approach of the study was discussed by all authors. SB and JC developed a first version of the analysis framework, and subsequently LM and JC expanded it and performed the numerical calculations and VVE wrote the text, with inputs from LM, JC, and EK. All authors discussed the results and commented on the manuscript.

<sup>3</sup> While DUNE and Hyper-Kamiokande do rely on matter effects, the neutrino beams that will be used for this measurement only traverse Earth's crust, with far better known properties than the deep mantle and core of the Earth.

## Funding

This research has benefited from the financial support of the CNRS Interdisciplinary Program 80PRIME, the LabEx UnivEarthS at Université Paris Cité (ANR-10-LABX-0023 and ANR-18-IDEX-0001).

## Acknowledgments

The authors acknowledge the support of Institut Universitaire de France, Université Paris Cité LabEx UnivEarthS, and CNRS Mission pour les Initiatives Transverses et Interdisciplinaires for conducting the research presented in this article.

## References

- Aartsen, M. G., Abraham, K., Ackermann, M., Adams, J., Aguilar, J. A., Ahlers, M., et al. (2017). Pingu: A vision for neutrino and particle physics at the south Pole. *J. Phys. G* 44, 054006. doi:10.1088/1361-6471/44/5/054006
- Abe, K., Aihara, H., Andreopoulos, C., Anghel, I., Ariga, A., Ariga, T., et al. (2015). Physics potential of a long-baseline neutrino oscillation experiment using a J-PARC neutrino beam and Hyper-Kamiokande. *PTEP* 2015, 053C02–0. doi:10.1093/ptep/ptv061
- Abe, K., Abe, K., Aihara, H., Aimi, A., Akutsu, R., Andreopoulos, C., et al. (2018). *Hyper-kamiokande design report*. doi:10.48550/arXiv.1805.04163
- Abe, Y., Aberle, C., Akiri, T., dos Anjos, J. C., Ardellier, F., Barbosa, A. F., et al. (2012). Indication of Reactor  $\bar{\nu}_e$  Disappearance in the Double Chooz Experiment. *Phys. Rev. Lett.* 108, 131801. doi:10.1103/physrevlett.108.131801
- Abi, B., Acciarri, R., and Acero, M. A. (2020a). Deep underground neutrino experiment (DUNE), far detector technical design report, Volume II: DUNE physics 2. doi:10.48550/arXiv.2002.03005
- Abi, B., Acciarri, R., Acero, M. A., Adamov, G., Adams, D., Adinolfi, M., et al. (2020b). Long-baseline neutrino oscillation physics potential of the DUNE experiment. *Eur. Phys. J. C* 80, 978. doi:10.1140/epjc/s10052-020-08456-z
- Abi, B., Acciarri, R., Acero, M., Adamov, G., Adams, D., Adinolfi, M., et al. (2020c). Volume I. Introduction to DUNE. *JINST* 15, T08008. doi:10.1088/1748-0221/15/08/T08008
- Adrián-Martínez, S., Ageron, M., Aiello, S., Albert, A., Ameli, F., Anassontzis, E. G., et al. (2017). Intrinsic limits on resolutions in muon- and electron-neutrino charged-current events in the KM3NeT/ORCA detector. *JHEP* 05, 008. doi:10.1007/JHEP05(2017)008
- Adrian-Martinez, S., Ageron, M., Aharonian, F., Aiello, S., Albert, A., Ameli, F., et al. (2016). Letter of intent for KM3NeT 2.0. *J. Phys. G* 43, 084001. doi:10.1088/0954-3899/43/8/084001
- Ahn, J. K., Chebotaryov, S., Choi, J. H., Choi, S., Choi, W., Choi, Y., et al. (2012). Observation of reactor electron antineutrinos disappearance in the RENO experiment. *Phys. Rev. Lett.* 108, 191802. doi:10.1103/physrevlett.108.191802
- Aiello, S., Albert, A., Alves Garre, S., Aly, Z., Ambrosone, A., Ameli, F., et al. (2022). Determining the neutrino mass ordering and oscillation parameters with KM3NeT/ORCA. *Eur. Phys. J. C* 82, 26. doi:10.1140/epjc/s10052-021-09893-0
- An, F., An, G., An, Q., Antonelli, V., Baussan, E., Beacom, J., et al. (2016). Neutrino physics with JUNO. *J. Phys. G* 43, 030401. doi:10.1088/0954-3899/43/3/030401
- An, F. P., Bai, J. Z., Balantekin, A. B., Band, H. R., Beavis, D., Beriguete, W., et al. (2012). Observation of electron-antineutrino disappearance at Daya Bay. *Phys. Rev. Lett.* 108, 171803. doi:10.1103/physrevlett.108.171803
- Andreopoulos, C., Bell, A., Bhattacharya, D., Cavanna, F., Dobson, J., Dytman, S., et al. (2010). The GENIE neutrino Monte Carlo generator. *Nucl. Instrum. Meth. A* 614, 87–104. doi:10.1016/j.nima.2009.12.009
- Badro, J., Brodtholt, J. P., Piet, H., Siebert, J., and Ryerson, F. J. (2015). Core formation and core composition from coupled geochemical and geophysical constraints. *PNAS* 112 (40), 12310–12314. doi:10.1073/pnas.1505672112
- Barr, G. D., Gaisser, T. K., Robbins, S., and Stanev, T. (2006). Uncertainties in atmospheric neutrino fluxes. *Phys. Rev. D* 74, 094009. doi:10.1103/PhysRevD.74.094009
- Birch, F. (1961). Composition of the earth's mantle. *Geophys. J. Int.* 4, 295–311. doi:10.1111/j.1365-246x.1961.tb06821.x
- Bourret, S., Coelho, J. A. B., and Van Elewycyk, V. (2018). Neutrino oscillation tomography of the Earth with KM3NeT-ORCA. *PoS ICRC2017*, 1020. doi:10.22323/1.301.1020
- Bourret, S., and Van Elewycyk, V. (2019). Earth tomography with neutrinos in KM3NeT-ORCA. *EPJ Web Conf.* 207, 04008. doi:10.1051/epjconf/201920704008
- Capozzi, F., Di Valentino, E., Lisi, E., Marrone, A., Melchiorri, A., and Palazzo, A. (2021). Unfinished fabric of the three neutrino paradigm. *Phys. Rev. D* 104, 083031. doi:10.1103/PhysRevD.104.083031
- Capozzi, F., and Petcov, S. T. (2022). Neutrino tomography of the Earth with ORCA detector. *Eur. Phys. J. C* 82, 461. doi:10.1140/epjc/s10052-022-10399-6
- Čerenkov, P. A. (1937). Visible radiation produced by electrons moving in a medium with velocities exceeding that of light. *Phys. Rev.* 52, 378–379. doi:10.1103/PhysRev.52.378
- de Salas, P. F., Forero, D. V., Gariazzo, S., Martínez-Miravé, P., Mena, O., Ternes, C. A., et al. (2021). 2020 global reassessment of the neutrino oscillation picture. *JHEP* 02, 071. doi:10.1007/JHEP02(2021)071
- Denton, P. B., and Pestes, R. (2021). Neutrino oscillations through the Earth's core. *Phys. Rev. D* 104, 113007. doi:10.1103/PhysRevD.104.113007
- D'Olivo, J. C., Herrera Lara, J. A., Romero, I., Sampayo, O. A., and Zapata, G. (2020). Earth tomography with atmospheric neutrino oscillations. *Eur. Phys. J. C* 80, 1001. doi:10.1140/epjc/s10052-020-08585-5
- D'Olivo Saez, J. C., Lara, J. A. H., Romero, I., and Sampayo, O. A. (2022). Oscillation tomography study of Earth's composition and density with atmospheric neutrinos. *Eur. Phys. J. C* 82, 614. doi:10.1140/epjc/s10052-022-10563-y
- Dziewonski, A. M., and Anderson, M. L. (1981). Preliminary reference Earth model. *Phys. Earth Planet. Int.* 25 (4), 297–356. doi:10.1016/0031-9201(81)90046-7
- Ermilova, V. K., Tsarev, V. A., and Chechin, V. A. (1986). Buildup of neutrino oscillations in the earth. *JETP Lett.* 43, 453–456.
- Esteban, I., Gonzalez-Garcia, M. C., Maltoni, M., Schwetz, T., and Zhou, A. (2020). The fate of hints: Updated global analysis of three-flavor neutrino oscillations. *JHEP* 09, 178. doi:10.1007/JHEP09(2020)178
- Freund, M. (2001). Analytic approximations for three neutrino oscillation parameters and probabilities in matter. *Phys. Rev. D* 64, 053003. doi:10.1103/PhysRevD.64.053003
- Fukuda, Y., Hayakawa, T., Ichihara, E., Inoue, K., Ishihara, K., Ishino, H., et al. (1998). Evidence for oscillation of atmospheric neutrinos. *Phys. Rev. Lett.* 81, 1562–1567. doi:10.1103/PhysRevLett.81.1562
- Giganti, C., Lavignac, S., and Zito, M. (2018). Neutrino oscillations: The rise of the PMNS paradigm. *Prog. Part. Nucl. Phys.* 98, 1–54. doi:10.1016/j.pnpnp.2017.10.001

## Conflict of interest

The authors declare that the research was conducted in the absence of any commercial or financial relationships that could be construed as a potential conflict of interest.

## Publisher's note

All claims expressed in this article are solely those of the authors and do not necessarily represent those of their affiliated organizations, or those of the publisher, the editors and the reviewers. Any product that may be evaluated in this article, or claim that may be made by its manufacturer, is not guaranteed or endorsed by the publisher.

- Hirose, S., Labrosse, K., and Hernlund, J. (2013). Composition and state of the core. *Annu. Rev. Earth Planet Sci.* 41, 657–691. doi:10.1146/annurev-earth-050212-124007
- Hofestädt, J., Bruchner, M., and Eberl, T. (2020). Super-ORCA: Measuring the leptonic CP-phase with atmospheric neutrinos and beam neutrinos. *PoS ICRC2019*, 911. doi:10.22323/1.358.0911
- Honda, M., Sajjad Athar, M., Kajita, T., Kasahara, K., and Midorikawa, S. (2015). Atmospheric neutrino flux calculation using the NRLMSISE-00 atmospheric model. *Phys. Rev. D* 92, 023004. doi:10.1103/PhysRevD.92.023004
- Huang, H., Fan, L., Liu, X., Xu, F., Wu, Y., Yang, G., et al. (2022). Inner core composition paradox revealed by sound velocities of Fe and Fe-Si alloy. *Nat. Commun.* 13, 616. doi:10.1038/s41467-022-28255-2
- Kaminski, E., and Javoy, M. (2013). A two-stage scenario for the formation of the Earth's mantle and core. *Earth Planet. Sci. Lett.* 365, 97–107. doi:10.1016/j.epsl.2013.01.025
- Kelly, K. J., Machado, P. A. N., Martinez-Soler, I., and Perez-Gonzalez, Y. F. (2022). DUNE atmospheric neutrinos: Earth tomography. *JHEP* 05, 187. doi:10.1007/JHEP05(2022)187
- Kumar, A., and Agarwalla, S. K. (2021). Validating the Earth's core using atmospheric neutrinos with ICAL at INO. *JHEP* 08, 139. doi:10.1007/JHEP08(2021)139
- Lindner, M., Ohlsson, T., Tomas, R., and Winter, W. (2003). Tomography of the Earth's core using supernova neutrinos. *Astropart. Phys.* 19, 755–770. doi:10.1016/S0927-6505(03)00120-8
- McDonough, W. F. (2003). Compositional model for the earth's core. *Elsevier* 2, 547–566.
- Mikheyev, S., and Smirnov, A. (1985). Resonance amplification of oscillations in matter and spectroscopy of solar neutrinos. *Sov. J. Nucl. Phys.* 42, 913–917.
- Nicolaidis, A., Jannane, M., and Tarantola, A. (1991). Neutrino tomography of the Earth. *J. Geophys. Res.* 96, 21811–21817. doi:10.1029/91JB01835
- Nicolaidis, A. (1988). Neutrinos for geophysics. *Phys. Lett. B* 200, 553–559. doi:10.1016/0370-2693(88)90170-0
- Ohlsson, T., and Winter, W. (2002). Could one find petroleum using neutrino oscillations in matter? *Europhys. Lett.* 60, 34–39. doi:10.1209/epl/i2002-00314-9
- Ohlsson, T., and Winter, W. (2001). Reconstruction of the Earth's matter density profile using a single neutrino baseline. *Phys. Lett. B* 512, 357–364. doi:10.1016/S0370-2693(01)00731-6
- Poirier, J.-P. (1994). Light elements in the earth's outer core: A critical review. *Phys. Earth Planet. Inter.* 85, 319–337. doi:10.1016/0031-9201(94)90120-1
- Rott, C., Taketa, A., and Bose, D. (2015). Spectrometry of the earth using neutrino oscillations. *Sci. Rep.* 5, 15225. doi:10.1038/srep15225
- Rubbia, C., Antonello, M., Aprili, P., Baibussinov, B., Ceolin, M. B., Barze, L., et al. (2011). Underground operation of the ICARUS T600 LAr-TPC: First results. *JINST* 6, P07011. doi:10.1088/1748-0221/6/07/P07011
- Rubbia, C. (1977). *The liquid argon time projection chamber: A new concept for neutrino detectors*. CERN Report CERN-EP-INT-77-08.
- Sakamaki, T., Ohtani, E., Fukui, H., Kamada, S., Takahashi, S., Sakairi, T., et al. (2016). Constraints on Earth's inner core composition inferred from measurements of the sound velocity of hcp-iron in extreme conditions. *Sci. Adv.* 2, e1500802. doi:10.1126/sciadv.1500802
- Sakamaki, T., Ohtani, E., Urakawa, S., Suzuki, A., and Katayama, Y. (2009). Measurement of hydrous peridotite magma density at high pressure using the x-ray absorption method. *Earth Planet. Sci. Lett.* 287, 293–297. doi:10.1016/j.epsl.2009.07.030
- Smirnov, O. (2019). Experimental aspects of geoneutrino detection: Status and perspectives. *Prog. Part. Nucl. Phys.* 109, 103712. doi:10.1016/j.pnpnp.2019.103712
- Suzuki, Y. (2001). Multimegaton water Cherenkov detector for a proton decay search: TITAND (former name TITANIC). *11th Int. Sch. Part. Cosmol.*, 288–296.
- Suzuki, Y. (2019). The Super-Kamiokande experiment. *Eur. Phys. J. C* 79, 298. doi:10.1140/epjc/s10052-019-6796-2
- Tagawa, S., Ohta, K., Hirose, K., Kato, C., and Ohishi, Y. (2016). Compression of Fe-Si-H alloys to core pressures. *Geophys. Res. Lett.* 43 (8), 3686–3692. doi:10.1002/2016gl068848
- Tagawa, S., Sakamoto, N., Hirose, K., Yokoo, S., Hernlund, J., Ohishi, Y., et al. (2021). Experimental evidence for hydrogen incorporation into Earth's core. *Nat. Commun.* 12, 2588. doi:10.1038/s41467-021-22035-0
- Tamm, I. E., and Frank, I. M. (1937). Visible radiation produced by electrons moving in a medium with velocities exceeding that of light. *Dokl. Acad. Sci. USSR* 14, 107–112. doi:10.1007/978-3-642-74626-0\_2
- Umemoto, K., and Hirose, K. (2015). Liquid iron-hydrogen alloys at outer core conditions by first-principles calculations. *Geophys. Res. Lett.* 42, 7513–7520. doi:10.1002/2015gl065899
- Winter, W. (2016). Atmospheric neutrino oscillations for earth tomography. *Nucl. Phys. B* 908, 250–267. doi:10.1016/j.nuclphysb.2016.03.033
- Winter, W. (2006). Neutrino tomography: Learning about the Earth's interior using the propagation of neutrinos. *Earth Moon Planets* 99, 285–307. doi:10.1007/s11038-006-9101-y
- Wolfenstein, L. (1978). Neutrino oscillations in matter. *Phys. Rev. D* 17, 2369–2374. doi:10.1103/PhysRevD.17.2369
- Yuan, L., and Steinle-Neumann, G. (2020). Strong sequestration of hydrogen into the earth's core during planetary differentiation. *Geophys. Res. Lett.* 47, e2020GL088303. doi:10.1029/2020gl088303